



Highly efficient holograms based on c-Si metasurfaces in the visible range

AUGUSTO MARTINS,¹ JUNTAO LI,^{2,4} ACHILES F. DA MOTA,¹ YIN WANG,² LUIZ G. NETO,¹ JOÃO P. DO CARMO,¹ FERNANDO L. TEIXEIRA,³ EMILIANO R. MARTINS,¹ AND BEN-HUR V. BORGES^{1,5}

¹Metamaterials Group (GMeta), Dept of Electrical Engineering, University of São Paulo, CEP 13566-590, São Carlos - SP, Brazil

²State Key Laboratory of Optoelectronic Materials and Technologies, School of Physics, Guangzhou, 510275, China

³ElectroScience Laboratory, The Ohio State University, Columbus, Ohio 43210, USA

⁴lijt3@mail.sysu.edu.cn

⁵benhur@sc.usp.br

Abstract: This paper reports on the first hologram in transmission mode based on a c-Si metasurface in the visible range. The hologram shows high fidelity and high efficiency, with measured transmission and diffraction efficiencies of ~65% and ~40%, respectively. Although originally designed to achieve full phase control in the range $[0-2\pi]$ at 532 nm, these holograms have also performed well at 444.9 nm and 635 nm. The high tolerance to both fabrication and wavelength variations demonstrate that holograms based on c-Si metasurfaces are quite attractive for diffractive optics applications, and particularly for full-color holograms.

© 2018 Optical Society of America under the terms of the [OSA Open Access Publishing Agreement](#)

OCIS codes: (090.1705) Color holography; (050.0050) Diffraction and gratings; (160.3918) Metamaterials; (160.5298) Photonic crystals; (090.1760) Computer holography

References and links

1. C. L. Holloway, E. F. Kuester, J. A. Gordon, J. O'Hara, J. Booth, and D. R. Smith, "An Overview of the Theory and Applications of Metasurfaces: The Two-Dimensional Equivalents of Metamaterials," *IEEE Antennas Propag.* **54**(2), 10–35 (2012).
2. P. Genevet and F. Capasso, "Holographic Optical metasurfaces: a review of current progress," *Rep. Prog. Phys.* **78**(2), 024401 (2015).
3. P. Genevet, F. Capasso, F. Aieta, M. Khorasaninejad, and R. Devlin, "Recent advances in planar optics: from plasmonic to dielectric metasurfaces," *Optica* **4**(1), 139–152 (2017).
4. N. Yu and F. Capasso, "Flat optics with designer metasurfaces," *Nat. Mater.* **13**(2), 139–150 (2014).
5. Y. Zhao, X.-X. Liu, and A. Alù, "Recent advances on optical metasurfaces," *J. Opt.* **16**(12), 123001 (2014).
6. F. Aieta, P. Genevet, N. Yu, M. A. Kats, Z. Gaburro, and F. Capasso, "Out-of-Plane Reflection and Refraction of Light by Anisotropic Optical Antenna Metasurfaces with Phase Discontinuities," *Nano Lett.* **12**(3), 1702–1706 (2012).
7. F. Aieta, P. Genevet, M. A. Kats, N. Yu, R. Blanchard, Z. Gaburro, and F. Capasso, "Aberration-Free Ultrathin Flat Lenses and Axicons at Telecom Wavelengths Based on Plasmonic Metasurfaces," *Nano Lett.* **12**(9), 4932–4936 (2012).
8. A. V. Kildishev, A. Boltasseva, and V. M. Shalaev, "Planar Photonics with Metasurfaces," *Science* **339**(6125), 1232009 (2013).
9. X. Ni, A. V. Kildishev, and V. M. Shalaev, "Metasurface holograms for visible light," *Nat. Commun.* **4**, 2807 (2013).
10. G. Zheng, H. Mühlenbernd, M. Kenney, G. Li, T. Zentgraf, and S. Zhang, "Metasurface holograms reaching 80% efficiency," *Nat. Nanotechnol.* **10**(4), 308–312 (2015).
11. W. Wan, J. Gao, and X. Yang, "Full-Color Plasmonic Metasurface Holograms," *ACS Nano* **10**(12), 10671–10680 (2016).
12. M. W. Knight, L. Liu, Y. Wang, L. Brown, S. Mukherjee, N. S. King, H. O. Everitt, P. Nordlander, and N. J. Halas, "Aluminum Plasmonic Nanoantennas," *Nano Lett.* **12**(11), 6000–6004 (2012).
13. Y.-W. Huang, W. T. Chen, W.-Y. Tsai, P. C. Wu, C.-M. Wang, G. Sun, and D. P. Tsai, "Aluminum plasmonic multicolor meta-hologram," *Nano Lett.* **15**(5), 3122–3127 (2015).
14. A. B. Evlyukhin, C. Reinhardt, and B. N. Chichkov, "Multipole light scattering by nonspherical nanoparticles in the discrete dipole approximation," *Phys. Rev. B* **84**(23), 235429 (2011).

15. I. Staude, A. E. Miroshnichenko, M. Decker, N. T. Fofang, S. Liu, E. Gonzales, J. Dominguez, T. S. Luk, D. N. Neshev, I. Brener, and Y. Kivshar, "Tailoring Directional Scattering through Magnetic and Electric Resonances in Subwavelength Silicon Nanodisks," *ACS Nano* **7**(9), 7824–7832 (2013).
16. M. Decker, I. Staude, M. Falkner, J. Dominguez, D. N. Neshev, I. Brener, T. Pertsch, and Y. S. Kivshar, "High-efficiency dielectric Huygens' surfaces," *Adv. Opt. Mater.* **3**(6), 813–820 (2015).
17. W. Zhao, H. Jiang, B. Liu, J. Song, Y. Jiang, C. Tang, and J. Li, "Dielectric Huygens' Metasurface for High-Efficiency Hologram Operating in Transmission Mode," *Sci. Rep.* **6**, 30613 (2016).
18. K. E. Chong, L. Wang, I. Staude, A. R. James, J. Dominguez, S. Liu, G. S. Subramania, M. Decker, D. N. Neshev, I. Brener, and Y. S. Kivshar, "Efficient polarization-insensitive complex wavefront control using Huygens' metasurfaces based on dielectric resonant meta-atoms," *ACS Photonics* **3**(4), 514–519 (2016).
19. A. Arbabi, Y. Horie, M. Bagheri, and A. Faraon, "Dielectric metasurfaces for complete control of phase and polarization with subwavelength spatial resolution and high transmission," *Nat. Nanotechnol.* **10**(11), 937–943 (2015).
20. Z. Zhou, J. Li, R. Su, B. Yao, H. Fang, K. Li, L. Zhou, J. Liu, D. Stellinga, C. P. Reardon, T. F. Krauss, and X. Wang, "Efficient Silicon Metasurfaces for Visible Light," *ACS Photonics* **4**(3), 544–551 (2017).
21. A. Zhan, S. Colburn, R. Trivedi, T. K. Fryett, C. M. Dodson, and A. Majumdar, "Low-contrast dielectric metasurface optics," *ACS Photonics* **3**(2), 209–214 (2016).
22. G. Yoon, D. Lee, K. T. Nam, and J. Rho, "Pragmatic Metasurface Hologram at Visible Wavelength: The Balance between Diffraction Efficiency and Fabrication Compatibility," *ACS Photonics* **4**, 7b01044 (2017).
23. A. Arbabi, R. M. Briggs, Y. Horie, M. Bagheri, and A. Faraon, "Efficient dielectric metasurface collimating lenses for mid-infrared quantum cascade lasers," *Opt. Express* **23**(26), 33310–33317 (2015).
24. M. Khorasaninejad, F. Aieta, P. Kanhaiya, M. A. Kats, P. Genevet, D. Rousso, and F. Capasso, "Achromatic metasurface lens at telecommunication wavelengths," *Nano Lett.* **15**(8), 5358–5362 (2015).
25. M. Khorasaninejad, W. T. Chen, R. C. Devlin, J. Oh, A. Y. Zhu, and F. Capasso, "Metalenses at visible wavelengths: Diffraction-limited focusing and subwavelength resolution imaging," *Science* **352**(6290), 1190–1194 (2016).
26. K. Huang, Z. Dong, S. Mei, L. Zhang, Y. Liu, H. Liu, H. Zhu, J. Teng, B. Luk'yanchuk, J. K. Yang, and C.-W. Qiu, "Silicon multi-meta-holograms for the broadband visible light," *Laser Photonics Rev.* **10**(3), 500–509 (2016).
27. Q.-T. Li, F. Dong, B. Wang, F. Gan, J. Chen, Z. Song, L. Xu, W. Chu, Y.-F. Xiao, Q. Gong, and Y. Li, "Polarization-independent and high-efficiency dielectric metasurfaces for visible light," *Opt. Express* **24**(15), 16309–16319 (2016).
28. B. Wang, F. Dong, Q.-T. Li, D. Yang, C. Sun, J. Chen, Z. Song, L. Xu, W. Chu, Y.-F. Xiao, Q. Gong, and Y. Li, "Visible-frequency dielectric metasurfaces for multiwavelength achromatic and highly dispersive holograms," *Nano Lett.* **16**(8), 5235–5240 (2016).
29. R. C. Devlin, M. Khorasaninejad, W. T. Chen, J. Oh, and F. Capasso, "Broadband high-efficiency dielectric metasurfaces for the visible spectrum," *Proc. Natl. Acad. Sci. U.S.A.* **113**(38), 10473–10478 (2016).
30. L. Wang, S. Kruk, H. Tang, T. Li, I. Kravchenko, D. N. Neshev, and Y. S. Kivshar, "Grayscale transparent metasurface holograms," *Optica* **3**(12), 1504–1505 (2016).
31. S. Kruk, B. Hopkins, I. I. Kravchenko, A. Miroshnichenko, D. N. Neshev, and Y. S. Kivshar, "Invited Article: Broadband highly efficient dielectric metadevices for polarization control," *APL Photonics* **1**(3), 030801 (2016).
32. M. I. Shalaev, J. Sun, A. Tsukernik, A. Pandey, K. Nikolskiy, and N. M. Litchinitser, "High-efficiency all-dielectric metasurfaces for ultracompact beam manipulation in transmission mode," *Nano Lett.* **15**(9), 6261–6266 (2015).
33. K. E. Chong, I. Staude, A. James, J. Dominguez, S. Liu, S. Campione, G. S. Subramania, T. S. Luk, M. Decker, D. N. Neshev, I. Brener, and Y. S. Kivshar, "Polarization-independent silicon metadevices for efficient optical wavefront control," *Nano Lett.* **15**(8), 5369–5374 (2015).
34. P. Lalanne, S. Astilean, P. Chavel, E. Cambriil, and H. Launois, "Blazed binary subwavelength gratings with efficiencies larger than those of conventional échelette gratings," *Opt. Lett.* **23**(14), 1081–1083 (1998).
35. J. P. Balthasar Mueller, N. A. Rubin, R. C. Devlin, B. Groever, and F. Capasso, "Metasurface Polarization Optics: Independent Phase Control of Arbitrary Orthogonal States of Polarization," *Phys. Rev. Lett.* **118**(11), 113901 (2017).
36. Y. F. Yu, A. Y. Zhu, R. Paniagua-Domínguez, Y. H. Fu, B. Luk'yanchuk, and A. I. Kuznetsov, "High-transmission dielectric metasurface with 2π phase control at visible wavelengths," *Laser Photonics Rev.* **9**(4), 412–418 (2015).
37. R. W. Gerchberg and W. O. Saxton, "A practical algorithm for the determination of phase from image and diffraction plane pictures," *Optik (Stuttg.)* **35**, 237–246 (1972).
38. L. G. Neto, "Optical real-time holograms using liquid crystal television and computer interactive design," Doctoral Thesis (Université Laval, Canada, 1995).
39. J. W. Goodman, *Introduction to Fourier Optics* (Roberts & Company Publishers, 2005), Vol. 2.
40. D. M. Whittaker and I. S. Culshaw, "Scattering-matrix treatment of patterned multilayer photonic structures," *Phys. Rev. B* **60**(4), 2610–2618 (1999).
41. D. E. Aspnes and A. Studna, "Dielectric functions and optical parameters of si, ge, gap, gaas, inp, inas, and insb from 1.5 to 6.0 eV," *Phys. Rev. B* **27**(2), 985–1009 (1983).
42. I. H. Malitson, "Refraction and Dispersion of Synthetic Sapphire," *J. Opt. Soc. Am.* **52**(12), 1377–1379 (1962).

43. H. Pang, S. Yin, Q. Deng, Q. Qiu, and C. Du, "A novel method for the design of diffractive optical elements based on the Rayleigh-Sommerfeld integral," *Opt. Lasers Eng.* **70**, 38–44 (2015).
44. F. Wyrowski, "Diffractive optical elements: iterative calculation of quantized, blazed phase structures," *J. Opt. Soc. Am. A* **7**(6), 961–969 (1990).

1. Introduction

Metasurfaces are subwavelength structures that allow control of phase, amplitude and/or polarization of light [1–5]. Earlier metasurfaces were based on metallic nanoresonators whose functionality relied on localized plasmon resonances (LPR) [3–11]. Unfortunately, LPRs suffer from high losses at visible wavelengths that hinder the metasurface efficiency when operating at transmission-mode [3,9,11–13]. For instance, the maximum reported efficiency for a transmission metasurface hologram based on LPR is about ~10% at near-infrared wavelengths [9]. Furthermore, LPR-based metasurfaces do not allow full-phase control ($0-2\pi$) through resonance frequency tuning for the same polarization between incident and transmitted fields [3]. In contrast, when operating in reflection mode, LPR-based metallic metasurfaces using Pancharatnam-Berry phase optical elements are not affected by these problems, resulting in diffraction efficiencies around 80% at near-infrared [10].

Recently, all-dielectric metasurfaces based on high refractive index materials have been proposed as an alternative to circumvent the low transmission problem of metallic metasurfaces. These all-dielectric metasurfaces can be divided into high- and low-contrast structures, with contrast defined as the difference between the refractive index of the nanoinclusion and that of the surrounding medium. High-contrast metasurfaces structured as low-aspect ratio resonators may exhibit only electric and magnetic dipolar Mie resonances at optical wavelengths [14], and these resonances can be tuned and brought into spectral overlap [15], thus allowing manipulation of light's amplitude and phase [16–18]. However, if both the contrast and aspect-ratio are high, the structure may exhibit several multipole resonances at optical wavelengths [14]. In this case, it is preferable to treat each structure as a truncated waveguide (exhibiting Fabry-Pérot resonances [19]) where the waveguide effective index can be tailored by adjusting the structure's fill-factor. This last feature offers an attractive degree-of-freedom in the design of diffraction gratings as it allows them to be made with either high or low index contrast. For instance, a $[0-2\pi]$ phase control has been achieved with tall cylinders (nanoposts) with high transmission [19–22]. In fact, the high diffraction efficiency provided by dielectric metasurfaces has been explored in many other classical applications, such as lenses [23–25], holograms [17–19,22,26–30], wave plates [31], anomalous refraction generation [20,32], and vortex beam generation [32,33].

The choice of materials, as expected, plays an important role in the structures design. High index materials such as titanium dioxide (TiO_2) [25,29,34,35], silicon nitride (Si_3N_4) [21], and silicon [17–20,26–28,30–32,36] are usually the preferred choice for this task. Silicon is particularly interesting for metasurface applications not only for its compatibility with CMOS processes, but also for its high refractive index that allows high-contrast gratings to be fabricated with low aspect ratio. For instance, metasurface holograms with diffraction efficiencies in excess of 90% were obtained in the infrared with poly-silicon (p-Si) metasurfaces based on Mie resonances [30] and with amorphous silicon (a-Si) based on high-contrast grating [19]. However, the high absorption of these two types of silicon severely limits their application in the visible range. For example, a full color hologram has been demonstrated with diffraction efficiencies of only 3.6%(blue), 5.2%(green) and 18% (red) [28] using amorphous silicon (a-Si). Furthermore, using poly-silicon (p-Si) a hologram operating at 532 nm has been demonstrated with a diffraction efficiency of only 6% [22].

In this scenario, crystalline silicon (c-Si) can be advantageous as it has lower absorption in the visible range. This feature motivated the recent demonstration of a polarization independent metasurface based on c-Si, which achieved a high transmission efficiency of 71% at 532 nm with an aspect ratio of only 3.4 [20]. In contrast, a TiO_2 -based metasurface hologram requires aspect ratios larger than 10 [29] to achieve similar efficiency.

Here, we exploit this combination of high transmission and low aspect ratio to demonstrate for the first time, to the best of our knowledge, a hologram based on a c-Si metasurface operating in the visible range and in transmission mode. The metasurface is designed for the wavelength of 532 nm with grating periodicity of 190 nm . The holograms are calculated via the modified Gerchberg-Saxton (G-S) phase-retrieval algorithm to maximize the signal-to-noise-ratio (SNR [37,38]). In our design, the radius of the c-Si nanoposts are modulated to achieve eight phase levels. We fabricate two different metasurfaces, each with a different number of nanoposts per pixel to investigate the effects of this parameter on the image efficiency and fidelity. All of our investigated designs are reconstructed numerically (prior to fabrication) using the Rayleigh-Sommerfeld (R-S) integral [39]. The measured transmission and diffraction efficiencies are as high as 65% and 40%, respectively.

We also investigate the performance of these metasurfaces, both numerically and experimentally, at 444.9 nm and 635 nm to assess their performance bandwidth. The reconstructed images at these wavelengths show good quality despite their expected reduced transmission efficiency and SNR. The measured average diffraction efficiencies reach $\sim 16\%$ (444.9 nm) and $\sim 25\%$ (635 nm), which are still higher than those obtained with a-Si [28] and p-Si [22]. Moreover, we verified that c-Si-based metasurfaces holograms are quite tolerant to fabrication and wavelength variations, thus making them attractive for diffractive optics applications and particularly for full-color holograms.

2. Metasurface design

The metastructure design is usually carried out with the help of a phase map obtained as a function of the structures geometrical parameters, for instance, of the aspect ratio and/or fill-factor. Each point in the phase map is obtained assuming an infinite array of identical nanoposts with aspect ratio and fill-factor defined according to their position in the map. The metasurface geometry is schematically shown in Fig. 1(a).

The phase level and transmission efficiency of the nanoposts are calculated using the rigorous coupled-wave analysis (RCWA) method [40]. As is well known, the number of phase levels strongly impacts the SNR at the reconstruction plane. In our design we adopt eight different phase levels and, consequently, eight different nanopost diameters. The selected eight phase (circles) and transmission (squares) values associated to the eight nanopost diameters are shown in Fig. 1. In order to assess the metasurface sensitivity to wavelength variations, we show the phase and transmission maps for three different wavelengths: for the target wavelength of 532 nm [Fig. 1(b)] which is the (designed) operating wavelength [Fig. 1(b)], for the wavelength of, 444.9 nm [Fig. 1(c)] and for the wavelength of 635 nm [Fig. 1(d)]. The complex refractive indexes of c-Si at 444.9 nm , 532 nm , and 635 nm are, respectively, $n = 3.875 + j0.0158$, $n = 4.141 + j0.032$ and $n = 4.733 + j0.099$ [41], with the index of sapphire substrate assumed constant ($n = 1.77$) [42]. As expected, $[0-2\pi]$ phase control with high transmission is obtained only at 532 nm . Despite the reduced phase control at 444.9 nm and 635 nm , the transmission values are still quite high at these wavelengths. Even though c-Si is highly absorbing in the visible, its extinction coefficient (imaginary part of the refractive index) is sufficiently low to be offset by the small geometrical dimensions of the silicon nanoposts (the extinction coefficient is about an order of magnitude lower in c-Si than in a-Si and p-Si). Consequently, the c-Si metasurface absorption is relatively low. The calculated phase and transmission efficiencies for the eight nanoposts are listed in Table 1 for all three wavelengths.

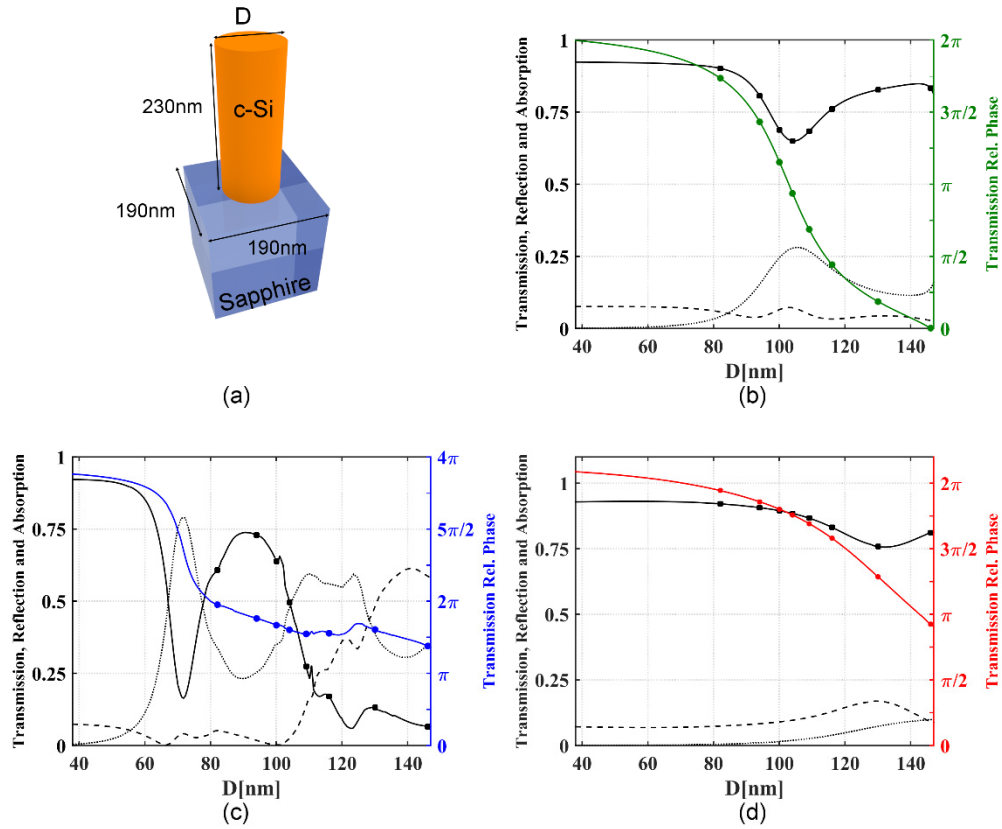


Fig. 1. (a) Schematic of the unit cell for the high contrast grating (not to scale). Transmission (black continuous), reflection (black dashed), absorption (black dotted) and relative phase (colored continuous) of the periodic c-Si posts shown as function of the post diameter at (b) 532 nm, (c) 444.9 nm and (d) 635 nm. Note that the post arrays are designed to operate at 532 nm (note the high transmission with full phase coverage in (b)). The dots show the eight selected phases and transmission values for each wavelength.

Table 1. Phase and transmission efficiencies of each pixel for the operating wavelength (532 nm) and two additional wavelengths, namely 444.9 nm and 632.8 nm.

	λ_0 (nm)	Post diameter (nm)							
		152	130	116	109	104	100	94	82
Phase [rad]	444.9	1.28π	1.50π	1.64π	1.68π	1.74π	1.80π	1.87π	2.01π
	532	0.00π	0.25π	0.50π	0.75π	π	1.25π	1.5π	1.75π
	635	0.93π	1.37π	1.64π	1.74π	1.80π	1.85π	1.90π	1.98π
Transmission	444.9	0.06	0.15	0.45	0.62	0.73	0.78	0.79	0.64
	532	0.85	0.80	0.68	0.65	0.65	0.65	0.68	0.80
	635	0.81	0.63	0.79	0.87	0.90	0.92	0.94	0.96

3. Optical characterization

The holograms are characterized with two different optical setups, one for reconstructing the hologram's image and other for measuring the transmitted and diffracted power. The first setup, shown in Fig. 2(a), consists of a solid-state laser, an iris (to block unwanted scattered

light by the optical interfaces), and two lenses (L_1 and L_2 with focus $f_1 = 7.5 \text{ cm}$ and $f_2 = 2.5 \text{ cm}$, respectively). The lenses are arranged as a Keplerian telescope to reduce the beam waist size to a collimated spot diameter of $\sim 400 \mu\text{m}$. All metasurfaces have an area of $389.12 \mu\text{m} \times 389.12 \mu\text{m}$. The reconstruction plane is located 20 cm away from the hologram in all cases. All reconstructions are captured with a camera (Nikon Coolpix p100) positioned in front of the reconstruction plane. The power measurement procedure is carried out as illustrated in Fig. 2(b), with the same optical source of (a), a lens L_3 ($f_3 = 25 \text{ cm}$), and an iris. The sample is positioned near the lens focus so that a beam waist of $\sim 200 \mu\text{m}$ is obtained (smaller than the hologram size) [10]. The total transmitted power is measured with the power meter detection head (Thorlabs S120C) positioned in front of the metasurface at position P_1 in Fig. 2(b) (this guarantees that the power is focused onto the detector surface). The zero-order transmitted power is measured by moving the detection head to the zero-order spot position represented by position P_2 in Fig. 2(b).

The metasurface is fabricated on a commercially available 230 nm thick c-Si (100) epitaxially grown on a sapphire substrate (from UniversityWafer, Inc.). The structure was patterned on a HSQ electron beam resist using electron beam generator Vistec EBPG 5000 + at 100 KeV . After developing the resist, the pattern was transferred from the resist into the silicon layer using inductively coupled plasma etching (PlasmaPro System 100ICP180). The remaining HSQ is removed with Hydrofluoric acid.

The c-Si layer is patterned as an array of circular nanoposts, which allows us to control the beam phase locally (by changing the nanoposts' diameter) with high transmission efficiency [19,20]. A 2π phase control is achieved with a unit cell size of 190 nm [20]. Figures 2(c) and 2(d) show a schematic of a metasurface hologram and a SEM micrograph of one of the fabricated metasurfaces, respectively.

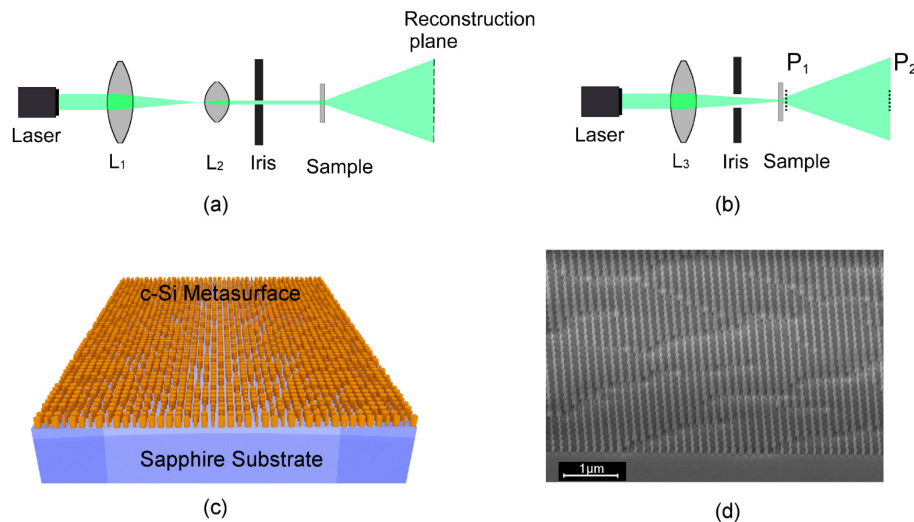


Fig. 2. (a) and (b) show the measurement setup used for the holograms's image reconstruction and power measurements, respectively. Note that in (a) the lenses L_1 and L_2 are arranged as a Keplerian telescope. (c) Schematic of a metasurface hologram and (d) SEM micrographs of a metasurface structure.

4. Results

In order to better assess the holograms performance, we investigate two different hologram designs with different resolutions and pixel sizes. The holograms target images are both shown in Fig. 3 (not to scale). The image window of Fig. 3(b) is centered at the reconstruction

plane, whereas that of Fig. 3(f) is phase-modulated to displace its reconstruction plane by 190 pixels vertically, thereby avoiding cross-talking with the unwanted zero-order and with the image's Hermitian that might occur due to imperfections in the phase modulation. Therefore, the zeroth order is seen in Fig. 3(b), but not in Fig. 3(f). Notice that the zeroth order of the hologram of Fig. 3(f) is not suppressed, it is only spatially separated from the image. It should be noted that this correction depends on several parameters related to the hologram design, such as pixel size, operating wavelength, propagation distance and image position in the reconstruction plane [43]. More details on the hologram design can be found in the methods section.

Each hologram is translated into a metasurface mask by correlating each phase level to a nanopost diameter according to Table 1. This procedure is performed for two configurations, as shown in Figs. 3(a) and 3(e). To improve the reconstructed image quality, each hologram is duplicated in both directions, forming a 2×2 hologram array, as shown in Figs. 3(a) and 3(e) [10]. Each configuration has a different combination of number of nanoposts per pixel, thus allowing the investigation of the effects of this parameter on the image efficiency and fidelity. The first hologram (target in Fig. 3(b)) is encoded on metasurface M1 [Fig. 3 (a)]. In this metasurface, each pixel consists of a 2×2 nanopost subarray. The second hologram (whose target is the wide-angle corrected image of Fig. 3(f)), on the other hand, is encoded on metasurface M2 [Fig. 3(e)] with only one nanopost per pixel. Note that M1 and M2 have the same size ($389.12 \mu\text{m} \times 389.12 \mu\text{m}$) but each hologram of the former is a 512×512 array of pixels with size of $380 \text{ nm} \times 380 \text{ nm}$ whereas each one of the latter is a 1024×1024 array with size of $190 \text{ nm} \times 190 \text{ nm}$. Therefore, the reconstruction of M2 requires the wide-angle correction because its reconstruction is wider (more details can be found in the methods section).

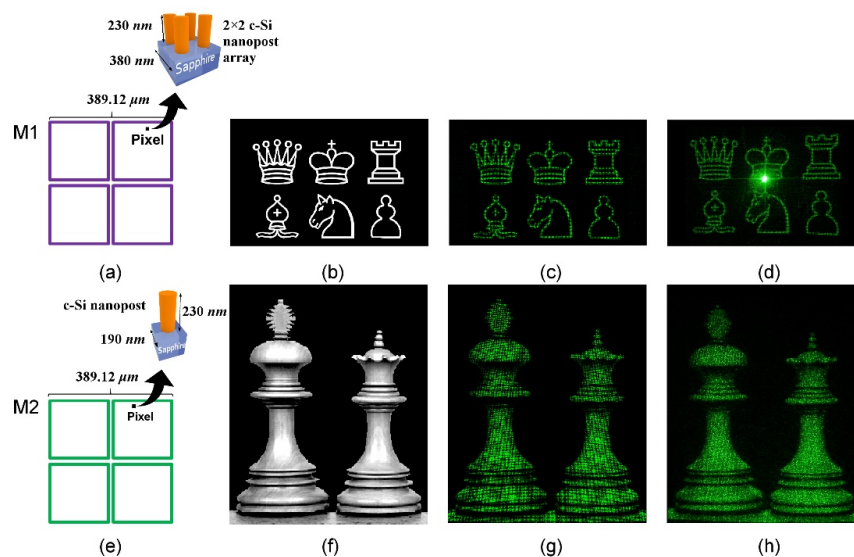


Fig. 3. (a) and (e) show the pictorial representation of the fabricated metasurface holograms M1 and M2, respectively. The insets in these figures show a representation of one individual pixel. All metasurfaces have dimensions of $389.12 \mu\text{m} \times 389.12 \mu\text{m}$. M1 encodes the hologram with 512×512 pixels, whose target image is shown in (b) and has 123×159 pixels. M1 is a 2×2 hologram array with pixel dimension of $380 \text{ nm} \times 380 \text{ nm}$ consisting of 2×2 nanopost subarray. M2 encodes the hologram with 1024×1024 pixels whose target image is shown in (j) with 257×213 pixels. It consists of a 2×2 hologram array with one nanopost per pixel with dimension $190 \text{ nm} \times 190 \text{ nm}$. (c) and (g) ((d) and (h)) show the numerical (experimental) image reconstructions from metasurfaces M1 and M2, respectively, taken 20 cm away from the hologram plane. The operating wavelength in all reconstructions is 532 nm . These figures are not to scale.

The holograms' numerical reconstruction is carried out via Rayleigh-Sommerfeld (R-S) integration with the reconstruction plane 20 cm away from the hologram. The reconstruction is carried out for the operating wavelength of 532 nm and also for the wavelengths of 444.5 nm and of 635 nm). These numerically reconstructed images are then used as benchmarks for performance comparison with the fabricated holograms. The numerical reconstructions follow two distinct approaches. One approach, which we call "c-Si metasurface", takes into consideration the variation of phase and amplitude in each pixel according to the values listed in Table 1. The other approach, which we call "Ideal", assumes constant field amplitude at the hologram, which is the ideal scenario. The transmission efficiency is defined as the ratio between the hologram's transmitted power to the transmitted power with the metasurface removed, and the diffraction efficiency is defined as the ratio between the power at the image window to the power transmitted with the metasurface removed.

Three main factors have an impact on the diffraction efficiency: 1) The amplitude and phase maps do not afford the ideal modulation required by the hologram. 2) The local character of the resonances: the amplitude and phase maps refer to infinite periodic arrays, but only a few periods are used in the metasurface to create the local resonance (often only a single period is used). Here, materials with high refractive index, such as c-Si, offer an obvious advantage, as they promote localization of the resonance. 3) Fabrication imperfections that induce noise in the phase and amplitude modulation.

The measured and calculated transmission and diffraction efficiencies are listed in Table 2 for all wavelengths. Note that the measured diffraction efficiency accounts for the energy outside the image window whereas the numerically calculated does not. As a result, the measured diffraction efficiency at 444.9 nm is higher than the numerical one due to the noise generated outside the image window, which is also accounted for in the measured diffraction efficiency. As theoretically predicted (see Tables 1 and 2), the transmission increases with wavelength for all cases. This behavior is also observed for the measured transmission and diffraction efficiencies. It is worth noting that the measured diffraction efficiencies are smaller than the numerical ones at the target wavelength of 532 nm, and the opposite is true for the transmission efficiencies. This is mostly because the fabricated metasurfaces have nanoposts whose diameters are on average 10 nm smaller than originally designed. Since the nanopost phase-diameter response is not linear [Fig. 1(b)], its relative phase is not maintained when the diameter is varied. The metasurface then loses more power to the zero order, therefore reducing its diffraction efficiency. Note that by modulating the pixel intensity via the c-Si nanopost array transmission reduces the diffraction efficiency by almost 20% for all metasurfaces at 532 nm (compare the c-Si and Ideal metasurfaces approaches in Table 2). Nonetheless, the diffraction efficiency is still high (around 50% for all samples) at this wavelength.

Table 2. Measured and calculated efficiencies at the holograms' reconstruction plane at different wavelengths. Note that the transmissions efficiencies of the Ideal Metasurfaces are all 100% and thus omitted from the table. The total efficiency is calculated integrating the field intensity radiated by each pixel.

Samples	c-Si – 230 nm					
	Experimental (Numerical) Transmission			Experimental (Numerical Ideal) Diffraction		
	444.9 nm	532 nm	635 nm	444.9 nm	532 nm	635 nm
M1	50.0 (53.1)	64.9 (72.0)	72.7 (85.1)	23.3 (16.2 72.6)	39.7 (52.2 72.9)	29.3 (39.8 71.9)
M2	41.7 (53.0)	62.9 (72.0)	77.0 (85.0)	18.3 (9.8 77.3)	33.1 (50.8 70.9)	25.7 (21.3 68.0)

Even though the phase control is worsened at 444.9 nm and 635 nm (see Table 1), the obtained transmission efficiencies still reach 53% and ~85%, respectively, for all samples, which is quite remarkable for the visible range and show the suitability of c-Si for metasurfaces operating in the visible. Note that the diffraction efficiencies at 444.9 nm and

632 nm are about half of those at 532 nm. This means that most of the transmitted energy does not contribute to the image reconstruction at these wavelengths, since it is essentially lost to the zero-order beam at the origin due to the poor phase modulation. Nevertheless, the holograms at the wavelengths of 444.9 nm and 632 nm still display relatively high brightness and quality, as shown in Fig. 4, which is an interesting observation given how far these wavelengths are from the target wavelength. These results show that holograms based on c-Si metasurfaces can be effectively applied for full-color holograms.

The numerical and experimental reconstructed images are shown in Fig. 3 (these figures are not to scale) operating at 532 nm. The other wavelengths' reconstructions are shown in Fig. 4, i.e., 444.9 nm (first two columns) and 635 nm (third and fourth columns). The reconstructions from sample M1 [Figs. 3(c)-3(d)] do not appear distorted even without wide-angle correction. This is due to its larger pixel size (2×2 array of nanoposts per pixel), which results in a smaller angular spread [39].

Sample M2, in turn, uses only one nanopost per pixel and wide-angle distortion correction [Figs. 3(g)-3(h)]. Observe that the correction performed in this sample is carried out only for the operation wavelength (532 nm), which makes the reconstructed images from it to appear distorted for the other wavelengths, namely 444.9 nm [Figs. 4 (c)-4(d)] and 632 nm [Figs. 4 (g)-4(h)]. Note how the image is warped at 444.9 nm (compare with Fig. 3 (f)). In this case, the reconstruction size is smaller than at 532 nm. Therefore, the wide-angle distortion is weaker and does not compensate for the correction performed previously on the target image. On the other hand, at 632 nm, the M2's reconstruction [Figs. 4 (g)-4(h)] is wider than at 532 nm and the wide-angle correction is not enough to compensate for the wide-angle distortion. Therefore, the reconstruction's image has a stretched aspect (compare with Fig. 3(f)).

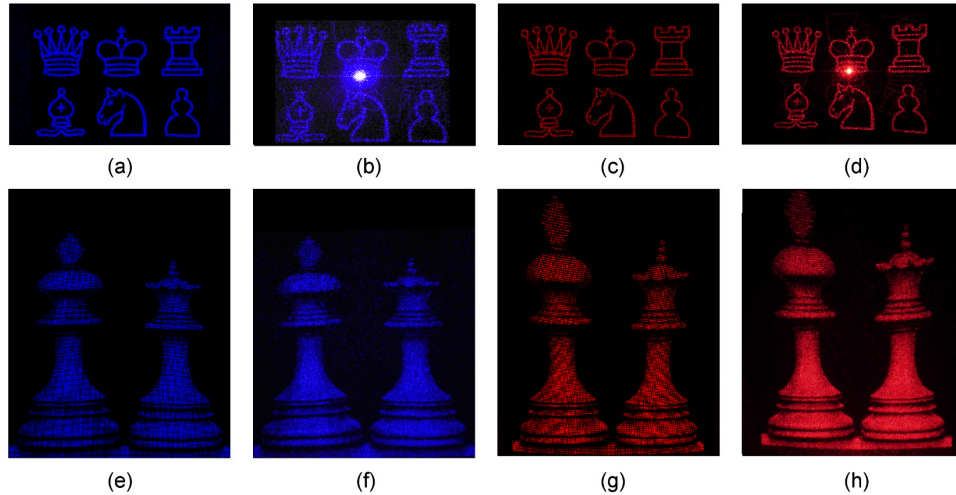


Fig. 4. Numerical and experimental image reconstructions from samples M1 (top row) and M2 (second row) taken 20 cm away from the hologram plane. The following wavelengths are used in these reconstructions: 444.9 nm (first two columns) and 635 nm (third and fourth columns). These figures are not to scale.

Finally, in order to quantify the hologram fidelity, we calculated the signal-to-noise ratio (SNR) of the proposed metasurfaces. This quantity is defined as

$$SNR = 10 \log_{10} \left(\frac{\sum_{\Omega} |M|^2}{\sum_{\Omega} (|I| - |M|)^2} \right) = 10 \log_{10} \left(\frac{1}{\sum_{\Omega} (|I| - |M|)^2} \right) \quad (1)$$

where Ω is the image window, I and M are the normalized field distributions of the ideal and c-Si metasurfaces, respectively. The sinc function that appears due to the zero-order diffraction at the origin is neglected in this calculation. It should be noted that both I and M are normalized in such a way that their power in Ω are the same (this is why the sum in the numerator equals 1). Thus, the mean squared error gives a measure of how much the metasurface reconstruction deviates from the ideal case without taking the intensity of the reconstructed image into account.

The results obtained with the SNR calculations are listed in Table 3. The SNR is larger than 34 for all cases at 532 nm, resulting in high reconstruction fidelity. This means that the amplitude modulation has little impact on the image reconstruction. In contrast, the SNR reach ~11 and ~10 at 444.9 nm and 635 nm, respectively.

Table 3. Signal-to-noise ratio (SNR) of the four metasurfaces investigated in this work at different wavelengths.

Samples	SNR		
	444.9 nm	532 nm	635 nm
M1	10.6	37.1	8.1
M2	11.2	34.8	10.6

5. Conclusions

We have presented for the first time a c-Si metasurface hologram designed to operate at 532 nm in transmission-mode with maximum transmission efficiency of ~65% and diffraction efficiency of ~40%. We have also investigated the performance of the metasurfaces, both numerically and experimentally at different wavelengths to assess their operation bandwidth. Surprisingly, the reconstructed images at these wavelengths show good quality despite their reduced theoretical transmission efficiency (~19% at 444.9 nm, and ~51% at 635 nm). We used the numerically reconstructed images, obtained with the Rayleigh-Sommerfeld integration, as benchmark to assess the performance of the fabricated metasurfaces in terms of transmission and diffraction efficiencies. The numerical calculations showed that the transmission(diffraction) efficiency can reach up to 53.1%(16.2%), 72%(52.2%) and 85%(39.8%) at 444.9 nm, 532 nm and 635 nm, respectively. There is plenty of room for improvements in future designs by optimizing of the metastructures at each wavelength. More importantly, these results show that c-Si-based hologram metasurfaces are tolerant to fabrication and wavelength variations, making them quite attractive not only for diffractive optics applications in general, but particularly for full-color holograms.

6. Methods

6.1 Hologram calculation

As is well known, the usual paraxial approximation required for Fresnel and Fourier diffraction calculations [39] hologram designs is not applicable when the pixels are subwavelength. At points far away from the center (assumed as the zero-order location in the screen) the R-S diffraction, which more realistically describes the actual diffraction, gets distorted. This problem can be circumvented with a wide-angle correction of the image during the hologram design [43]. Normally, the far-field profile is obtained by Fourier transforming the near field, as is usually done in Fourier diffraction. However, this procedure assumes the far-field sufficiently far away from the near-field so that its projection plane can be calculated as a spherical surface whose origin is at the hologram position. In the Fourier diffraction it is further assumed that the projection plane is planar, which is valid only in the paraxial approximation. Therefore, if the hologram is calculated using the Fourier transform and its period is small enough for the paraxial approximation to be used, the reconstruction will be

formed at the surface of a sphere and not at a planar screen as we would expect. This issue can be overcome by mapping the target image onto a spherical surface in the hologram design via a coordinate transformation [43]. This causes the reconstruction on a spherical surface to be distorted but it correctly reconstructs the image on a planar screen.

The holograms are calculated with the G-S phase-retrieval algorithm, from which eight phase levels are chosen [37,38]. In this algorithm, the field distribution at the reconstruction and hologram planes are numerically represented by two square matrices with equal number of pixels but larger than that of the target image. The target image is inserted in the reconstruction plane matrix in a region called image window with all unoccupied positions initialized as zero. For instance, the designed hologram of Fig. 3(b) has 123×159 and 512×512 pixels at the image window and reconstruction plane, respectively, while that of Fig. 3(j) has 257×213 and 1024×1024 , respectively. Then, a random phase noise is added to this field distribution followed by the calculation of the inverse Fourier diffraction of the resulting matrix. We use the inverse Fast-Fourier transform (IFFT) to obtain the matrix representing the field distribution at the hologram plane. The phase of the matrix at the hologram plane is quantized while the amplitude is normalized to a constant value. Subsequently, the field at the hologram position is Fast Fourier transformed (FFT) to the reconstruction plane [37,38]. The resulting matrix (containing the hologram's reconstructed field with quantized phases and normalized amplitudes) is then reinforced at the image window with the original image multiplied by a scale factor, therefore increasing the SNR [38]. The reinforcement is carried out iteratively via an iterative Fourier transform algorithm (IFTA [38]) until the phase quantization is complete. The phase quantization at the hologram's plane is not carried out in one step [44]. Instead, it makes use of a stepwise operator that restricts the allowed phase values on the hologram in each iteration. In the first iteration, all possible phase levels are allowed and the number of levels is iteratively reduced until a discrete number of values is obtained [44]. This process increases the algorithm's degree-of-freedom resulting in better efficiency and SNR [38,44]. The IFTA is carried out until the SNR is maximized.

Funding

São Paulo Research Foundation (FAPESP) (2015/21455-1, 2013/07276-1, 2016/05809-0, FAPESP/OSU 2015-AWARD 2015/50268-5); National Science Foundation of China (NSFC) (11674402, 11761131001, 91750207).

Acknowledgments

The authors would like to acknowledge the computing time provided on the DaVinci cluster supported by the Center for Research Computing (Rice University) and Superintendência de Tecnologia da Informação da Universidade de São Paulo.